Materials Today Bio 26 (2024) 101076

Contents lists available at ScienceDirect

Materials Today Bio

journal homepage: www.journals.elsevier.com/materials-today-bio

A multifunctional ionic liquid coating on 3D-Printed prostheses: Combating infection, promoting osseointegration

Zuhao Li [a,b,c,1], Lunqiang Jin [d,1], Xijing Yang [e], He Liu [c], Shengxu Qian [a], Zhonghan Wang [c], Jiaqi Liu [c], Jingxia Wang [f], Junjun Chen [a], Baihai Su [d], Chaorong Peng [f], Jincheng Wang [c,**], Zhenqiang Shi [a,*]

[a] School of Bioengineering, Dalian University of Technology, Dalian 116024, China
[b] Department of Orthopaedics, Xinhua Hospital Affiliated to Shanghai Jiaotong University School of Medicine, Shanghai 200092, China
[c] Orthopaedic Medical Center, The Second Hospital of Jilin University, Changchun 130041, China
[d] Department of Nephrology, West China Hospital of Sichuan University, Chengdu, 610041, China
[e] Animal Experiment Center, West China Hospital, Sichuan University, Chengdu 610041, China
[f] Radiation Chemistry Department, Sichuan Institute of Atomic Energy, Chengdu 610101, China

ARTICLE INFO

Keywords:
3D printing
Prosthesis
Ionic liquid
Periprosthetic infection
Osseointegration

ABSTRACT

Periprosthetic infection and mechanical loosening are two leading causes of implant failure in orthopedic surgery that have devastating consequences for patients both physically and financially. Hence, advanced prostheses to simultaneously prevent periprosthetic infection and promote osseointegration are highly desired to achieve long-term success in orthopedics. In this study, we proposed a multifunctional three-dimensional printed porous titanium alloy prosthesis coated with imidazolium ionic liquid. The imidazolium ionic liquid coating exhibited excellent bacterial recruitment property and near-infrared (NIR) triggered photothermal bactericidal activity, enabling the prosthesis to effectively trap bacteria in its vicinity and kill them remotely via tissue-penetrating NIR irradiation. *In vivo* anti-infection and osseointegration investigations in infected animal models confirmed that our antibacterial prosthesis could provide long-term and sustainable prevention against periprosthetic infection, while promoting osseointegration simultaneously. It is expected to accelerate the development of next-generation prostheses and improve patient outcomes after prosthesis implantation.

1. Introduction

Over the past few decades, the demand for orthopedic implants has significantly increased due to the aging population and the high incidence of trauma [1]. While various bone implants have been developed, periprosthetic infection remains a major factor leading to implant failure [2,3]. It has been reported that periprosthetic infection is the leading cause of repeated revision surgeries in arthroplasty [4], accounting for 20.4 % of implantation failures [5]. Once bacterial infection occurs on prostheses, osseointegration are highly impaired by severe inflammatory responses, suspecting to implant failure and even osteomyelitis [6,7], which are devastating consequences for patients both physically and financially. Therefore, it is of great significance to develop advanced implants with desirable biofunctions to prevent bacterial infections and accelerate osseointegration simultaneously to improve the service life of the prosthesis after implantation.

Titanium (Ti) and Ti-alloy have achieved great success in the field of orthopedic implants [8], because of their desirable mechanical compatibility, chemical stability, and biocompatibility [9]. The emerging three-dimensional (3D) printing technology further advances the capabilities of Ti-based biomaterials to an unparalleled level in bone repair. It offers revolutionary improvements in the flexibility in implant design to realize the creation of precisely customized shapes and structures of implants that are tailored to individual anatomical characteristics, enabling perfect geometry and mechanics match to prevent later-stage implant loosening [10–13]. Currently, customized 3D-printed porous titanium alloy (pTi) implants have achieved great success in anatomical reconstruction and functional recovery. Clinical

* Corresponding author.
** Corresponding author.
E-mail addresses: wangjinc@jlu.edu.cn (J. Wang), zhenqiangshi@dlut.edu.cn, shizhenqiang1992@163.com (Z. Shi).
[1] These authors contributed equally to this work.

https://doi.org/10.1016/j.mtbio.2024.101076
Received 18 January 2024; Received in revised form 27 March 2024; Accepted 27 April 2024
Available online 28 April 2024

studies have reported that personalized 3D-printed implants match bone defects perfectly, promote bone ingrowth, provide stable mechanical support, and improve functional scores with fewer complications [14–16].

Despite these advantages, periprosthetic infection, which is one of the most prevalent and challenging issues associated with implant materials, unfortunately remains unaddressed for titanium-based biomaterials. As a classical bioinert material, titanium and its alloys lack inherent antibacterial activity to fight against implant related infections [17,18]. Meanwhile, the porous structure brought by 3D printing not only contributes to cell penetration and nutrient transport to promote angiogenesis and induce bone ingrowth, but it also provides a favorable environment for bacterial colonization and proliferation [19]. Therefore, it is of great practical significance to endow pTi implants with satisfying superior antibacterial properties to intervene the race between bone tissue cells and bacteria for the implant surfaces.

Current antibacterial strategies can be broadly categorized into two main types: antifouling surfaces, which aim to inhibit bacterial adhesion, and bactericidal surfaces, which work to kill bacteria. Dull antifouling surfaces are not favorable for tissue engineering, as the *blind* repelling strategy fails to precisely regulate the surface adhesion behavior of bacteria and tissue cells to improve osseointegration. Thus, current strategies in bone repair rely heavily on the extensive use of antibiotics and other bactericidal agents toward bactericidal surfaces [20,21], either through drug delivery systems [6,22–24] or surface drug immobilization [25,26]. Unfortunately, hardly could any of the reported bactericidal strategies provide sufficient and sustainable antibacterial activities to cover the whole course of bone tissue regeneration (typically several months), due to either the limited reservoir capacity or the shielding effect of bacteria debris. As a result, there is a critical need for precise and sustainable approaches to effectively balance the seemingly contradictory bacterial infection and osseointegration.

In this study, based on an imidazolium ionic liquid coating, we developed a multifunctional 3D-printed pTi prosthesis with photothermal bactericidal activity to kill bacteria physically and sustainingly. The surface coating method could endow the 3D-printed pTi prosthesis with desired antibacterial properties without altering its native structure or damaging mechanical properties, which is crucial for prostheses for bone repair [27]. Meanwhile, the ionic liquid coating on the prosthesis surface exhibited interesting antibacterial activity. That is, to trap the bacteria surrounding the implants, and subsequently kill them on demand and in situ through remote near-infrared (NIR) irradiation, which exhibits excellent tissue penetration (Scheme 1). As no antibiotics or invasive revision surgery would be involved throughout the whole process, we believe that the multifunctional prosthesis proposed herein would accelerate the development of next-generation prostheses in infection prevention and osseointegration.

2. Materials and methods

2.1. Preparation of the 3D-printed porous titanium alloy prosthesis (pTi)

The 3D-printed pTi prosthesis was manufactured by the Arcam Electron Beam Melting (EBM) system (Q10, Sweden), following the method described in our previous studies [28–30]. Briefly, spherical titanium alloy powder (Ti6Al4V, Grade 23, particle size 45–100 μm, AK Medical Co., Ltd., Beijing, China) was melted layer-by-layer according to the preset parameters (pore size: 600 μm, porosity: 70 %, strut size: 300 μm). The 3D-printed pTi macroscopic shapes were either disk-shaped (φ10 mm × L3 mm) for *in vitro* experiments or columnar-shaped (φ6 mm × L10 mm) for *in vivo* investigations. All fabricated pTi were ultrasonically cleaned and washed sequentially in acetone, ethyl alcohol, and deionized water for 15 min for each procedure, and sequentially autoclaved for 30 min.

2.2. Preparation of the ionic liquid-coated pTi prosthesis (pTi@MMIB)

An ionic liquid of 3-(12-mercaptododecyl)-1-methyl-1*H*-imidazole-3-ium bromide (MMIB) was first synthesized (a detailed description is provided in the Supplementary Information). Then, the ionic liquid coating on the pTi prosthesis was prepared as follows: pTi prostheses were immersed in a dopamine hydrochloride solution (2 mg/mL in Tris–HCl buffer, pH = 8.5), and incubated at room temperature for 12 h under shaking. The polydopamine (PDA) coated prostheses were rinsed several times in ultrapure water for further modification. Triethylamine (820 μL, 6 mmol) was added to 50 mL of ethanol solution and bubbled with N_2 for 30 min. MMIB (1.82 g, 5 mmol) was then added under an atmosphere of N_2 (0.1 M in the coating solution), to ensure that its immobilization quantity reached saturation on the PDA layer. Subsequently, the PDA-coated prostheses were immersed into the above solution under shaking for 16 h at room temperature, and rinsed several times in ultrapure water. The as-prepared ionic liquid-coated prostheses

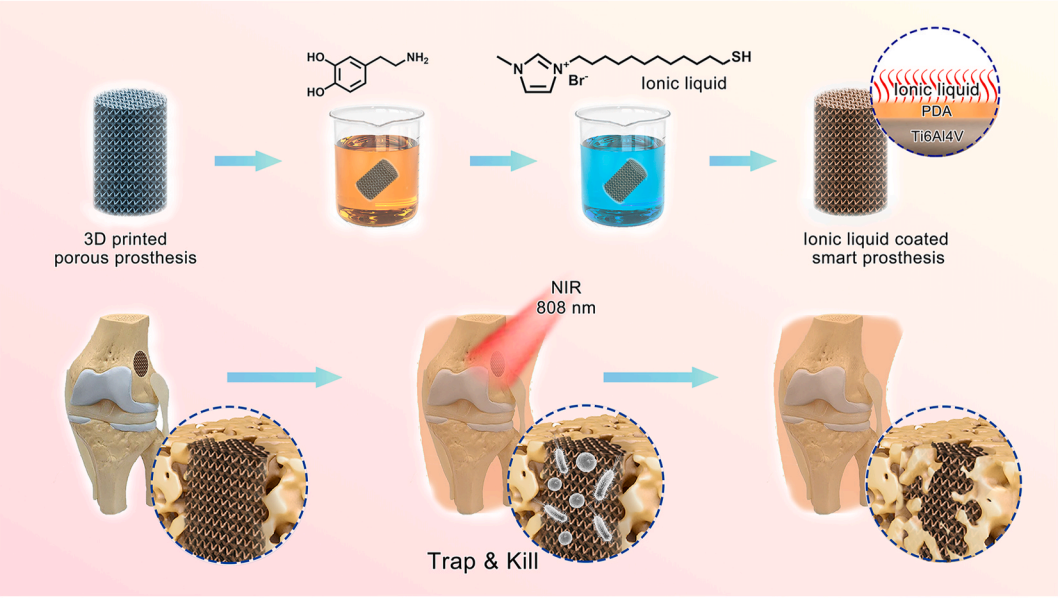

Scheme 1. Ionic liquid-coated 3D-printed prosthesis prevents periprosthetic infection and promotes osseointegration simultaneously.

were named pTi@MMIB.

2.3. Characterizations of the pTi@MMIB

Scanning electron microscopy (SEM, INSPECT F, FEI, Netherlands) was carried out for the morphology of the prostheses, and elemental mapping and energy dispersive spectroscopy (EDS) analysis were performed as well. Atomic force microscopy (AFM, Dimension Icon AFM, Bruker), and contact angle measurement (Drop Shape Analyzer, DSA25, KRÜSS) were carried out for the characterization of the ionic liquid coating. To facilitate the measurements, a flat titanium alloy (Ti6Al4V) substrate was applied for the ionic liquid coating modification, using the same method as for preparation of the pTi@MMIB, and the surface morphology, roughness, and wettability were then characterized. NIR photothermal conversion property of the pTi and pTi@MMIB prostheses were also assessed. The temperature changes of the dry prostheses when exposed to 808 nm NIR irradiation (2 W cm^{-2}) in an air environment was monitored, using a thermal imaging camera (Fluke, USA).

2.4. NIR-triggered photothermal antibacterial therapy

UV-sterilized prostheses were incubated in 5 mL of *Escherichia coli* (*E. coli*, ATCC 25922) or *Staphylococcus aureus* (*S. aureus*, ATCC 25923) suspension (1.0×10^5 CFU/mL) at 37 °C for 1 h. Then, the samples were irradiated with 808 nm NIR (2 W cm^{-2}) for 5 min. Following the NIR irradiation, the viability of the bacteria adhered to the prostheses was promptly assessed to evaluate their survival. Briefly, the prosthesis was fully immersed in 5 mL of normal saline. The adhered bacteria were subsequently dislodged from the prostheses and transferred to the normal saline solution using pulsed ultrasound (the pulsed ultrasound treatment involved 30 s of ultrasound followed by a 30 s pause in an ice-water bath, repeated for a total of 5 cycles). After that, the number of live bacteria in the solution was determined through the standard plate counting method, and the viability of the bacteria adhered to the prostheses could be calculated accordingly. The morphology of the bacteria on the prostheses was characterized by scanning electron microscopy (Nova NanoSEM 450, FEI, USA).

2.5. Biocompatibility assays

Rabbit bone marrow mesenchymal stem cells (rBMSCs, LM-Rb007) were used to evaluate the cytotoxicity of the ionic liquid coating and photothermal treatment. Briefly, rBMSCs were cultured in 24-well plates at a density of 2×10^4 cell/well, and 3D-printed prostheses were added to the wells. Two hours before detection, two groups, pTi + NIR and pTi@MMIB + NIR, were irradiated with 808 nm NIR (2 W cm^{-2}) for 60 s, while the other two groups, pTi and pTi@MMIB, were not irradiated. Cells were cultured in DMEM with 10 % FBS and 1 % penicillin–streptomycin under a humidified atmosphere of 5 % CO_2 at 37 °C in an incubator. The medium was refreshed every 3 days during cell culture.

At scheduled time points, CCK-8 assays were performed to evaluate cell proliferation according to the manufacturer's instructions. Briefly, the medium was replaced with 1 mL of fresh DMEM, and 10 % CCK-8 reaction solution was added into each well and incubated for 2 h at 37 °C. After that, 100 μL of sample solution was transferred to a 96-well plate and measured by a microplate reader (Multiskan EX, Thermo Fisher Scientific, MA, USA) at 450 nm. Calcein-AM/PI staining was also conducted to assess cell viability. Briefly, the samples were stained with calcein-AM (5 μM) and PI (2 μM) at 37 °C for 15 min in the dark, repeatedly washed with PBS and observed under a confocal laser scanning microscope (CLSM, FV1000, Olympus, Japan).

2.6. Preparation of periprosthetic infection models

All animal procedures were examined and approved by the Animal Ethics Committee of Jilin University (No. 20200169). A total of 40 New Zealand white rabbits (female, five months old) were incorporated into the *in vivo* investigation of periprosthetic infection and osseointegration. The implantation operation was carried out under general anaesthesia by 3 % (w/v) pentobarbital at a dose of 50 mg/kg. Carprofen was administered once a day at a dose of 4 mg/kg as the analgesic. Briefly, by making an incision through the lateral approach of the left knee, the soft tissue was separated layer by layer to expose the surface of the lateral condyle, and then a cylindrical bone defect with 6 mm diameter and 10 mm depth was created using a bone drill. After washing the area with normal saline to remove the bone slag, columnar-shaped pTi or pTi@MMIB prosthesis (φ6 mm × L10 mm) was implanted into the defect. Then, 500 μL of bacterial suspension containing 1.0×10^5 CFU *S. aureus* and *E. coli* was injected into the medullary cavity through the defects. The incision was sutured layer by layer using absorbable sutures. No antibiotics were administered postoperatively. The sample size of animals in each group was ten. The pTi + NIR and pTi@MMIB + NIR groups were irradiated with NIR (808 nm, 2 W cm^{-2}, 60 s) at the 1st, 3rd, 5th, 7th, 9th and 11th weeks after implantation, while the pTi and pTi@MMIB groups were not irradiated throughout the experiments. At the 12th week after implantation, animals were euthanized by 3 % (w/v) pentobarbital at a dose of 150 mg/kg. Samples of the distal femur and surrounding tissues were collected for subsequent detections.

2.7. Anti-infection evaluation in vivo

To evaluate systemic infection, peripheral blood was drawn through the vein at 2nd, 4th, 6th, 8th, 10th and 12th weeks after implantation for white blood cell (WBC) count. Besides, to detect the infection around the prosthesis interfaces at week 12, the tissue on the surface of prosthesis was collected, and stained with Giemsa staining to visualize the bacterial infection.

2.8. Micro computed tomography (Micro-CT)

To study bone formation around the prosthesis interfaces, the samples of distal femur were scanned by Micro-CT (90 kV voltage, 114 mA current, 18 μm pixel size). The cylindrical region of the prosthesis was selected as the region of interest for 3D reconstruction and quantitative morphometric analysis by Micro-CT auxiliary software (NRecon version 1.6.6).

2.9. Histological observation

All animals were intramuscularly injected with calcein at a dose of 8 mg/kg, on the 14 and 4 days before sacrifice, to detect the mineral apposition rate (MAR). Three months after pTi implantation, the left distal femur samples were harvested and preserved in a 4 % polyformaldehyde solution. The bone samples were embedded in methyl methacrylate without decalcification, and then sectioned into 150–300 μm slices. The slices were ground down and polished to 40–50 μm. The samples were observed under a CLSM, and MAR (μm/day) = IrL.Wi/interval, IrL.Wi represents the interlabel width (μm). And then the sections were stained with Masson's trichrome to observe the bone ingrowth.

2.10. Push-out test

To evaluate the osseointegration, the bond strength at the bone–prosthesis interface was tested via a standard push-out test with the AG-A20 KNA dynamic testing machine (Shimadzu, Nakagyo-ku Kyoto, Japan). Briefly, the distal femur samples were fixed on the experimental platform, and the indenter is pushed in parallel along the long axis of the interfaces at 0.1 mm/s. The peak push-out force was recorded as the point at which the interface detached from the bone.

2.11. Statistical analysis

All results are presented as the mean ± standard deviation. Comparisons among groups were analysed with one-way ANOVA followed by Tukey's post hoc test using SPSS 19.0 (SPSS Inc., Chicago, USA). All experiments were repeated independently at least three times. *p < 0.05, **p < 0.01, and ***p < 0.001.

3. Results and discussion

3.1. Characterization of the pTi@MMIB

Firstly, the porous scaffold substrate of pTi was fabricated through 3D printing technology. It is reported that porosity and pore size distribution are closely related to the osseointegration ability of orthopedic implants. Microporous prostheses with a diameter of 300–700 μm are conducive to cell adhesion, proliferation, and osteogenic differentiation in bone tissue engineering. The porosity of the porous scaffolds should be above 50 %, especially within 65–75 %, to accurately mimicking the structure and mechanics of human trabecular bone, thereby enhancing the bionic effect of the prosthesis [31,32]. In this study, taking advantage of 3D printing technology that offers revolutionary flexibility for the precision manufacturing, disk- and columnar-shaped pTi prostheses with designed parameters of 600 μm pore size and 70 % porosity were successfully prepared (Fig. S1). SEM images (Fig. 1a) demonstrated the homogeneous and porous network microstructure of the obtained pTi prosthesis. The interconnected microstructure would benefit cell penetration and nutrient transport, promoting angiogenesis and induce bone ingrowth [33,34]. Besides, the microstructure increased the surface roughness and specific surface area to enhance the prosthesis–bone interaction and initial stability, so that the micro-movements at the interface could be minimized.

To endow the pTi prosthesis with antibacterial activity to fight against periprosthetic infections, a novel imidazolium ionic liquid was immobilized to the prosthesis surface. Through an extensive structure-activity relationship study involving a range of ionic liquids, MMIB was specifically designed and chosen due to its advantageous combination of antibacterial activity and cytocompatibility (the minimal inhibitory concentrations of MMIB against *S. aureus* and *E. coli* are 4 and 8 μg/mL, respectively, and it demonstrated non-cytotoxicity at 200 μg/mL). Polydopamine (PDA), known for its substrate-independent adhesion property, served as a bioglue for coating the prostheses. Subsequently, MMIB is immobilized onto the PDA coating via a Michael addition reaction between the terminated thiol group in the imidazolium ionic liquid and the o-quinone groups in PDA [35], resulting in the fabrication of the pTi@MMIB prosthesis.

As shown in Fig. 1a and **b**, after the ionic liquid coating, the roughness of the prosthesis surface increased, and the color of the pTi@MMIB prostheses surface turned dark brown. However, the micro- and macro-structure of the 3D printed pTi prosthesis remained unchanged. More importantly, the ionic liquid coating showed a negligible effect on the mechanical properties of the prosthesis, which is more critical for orthopedic implants. The compressive strength and elastic modulus values were 48.0 ± 2.1 MPa and 1.6 ± 0.2 GPa, respectively. Elemental mapping demonstrated the uniform distribution of MMIB on the prosthesis surface, as indicated by the distribution of its characteristic element of S (Fig. 1c). Quantitative analysis revealed the increased relative atomic contents of C and S after the coating (Table 1). These results indicated the successful modification of the prosthesis surface. Atomic force microscopy (AFM) analysis on a flat Ti6Al4V substrate (Fig. 1d) further confirmed the slight increase in surface roughness (R_a) from 30.6 to 44.9 nm after the coating, and the thickness of the coating was measured to be ~2 μm using the scratch method (Fig. S2). Besides,

Table 1
Elemental compositions on the prosthesis surfaces determined by EDS.

sample	relative atomic content (%)				
	Ti	Al	V	C	S
pTi	71.2	8.4	4.2	16.2	0.0
pTi@MMIB	54.6	6.1	3.2	35.8	0.3

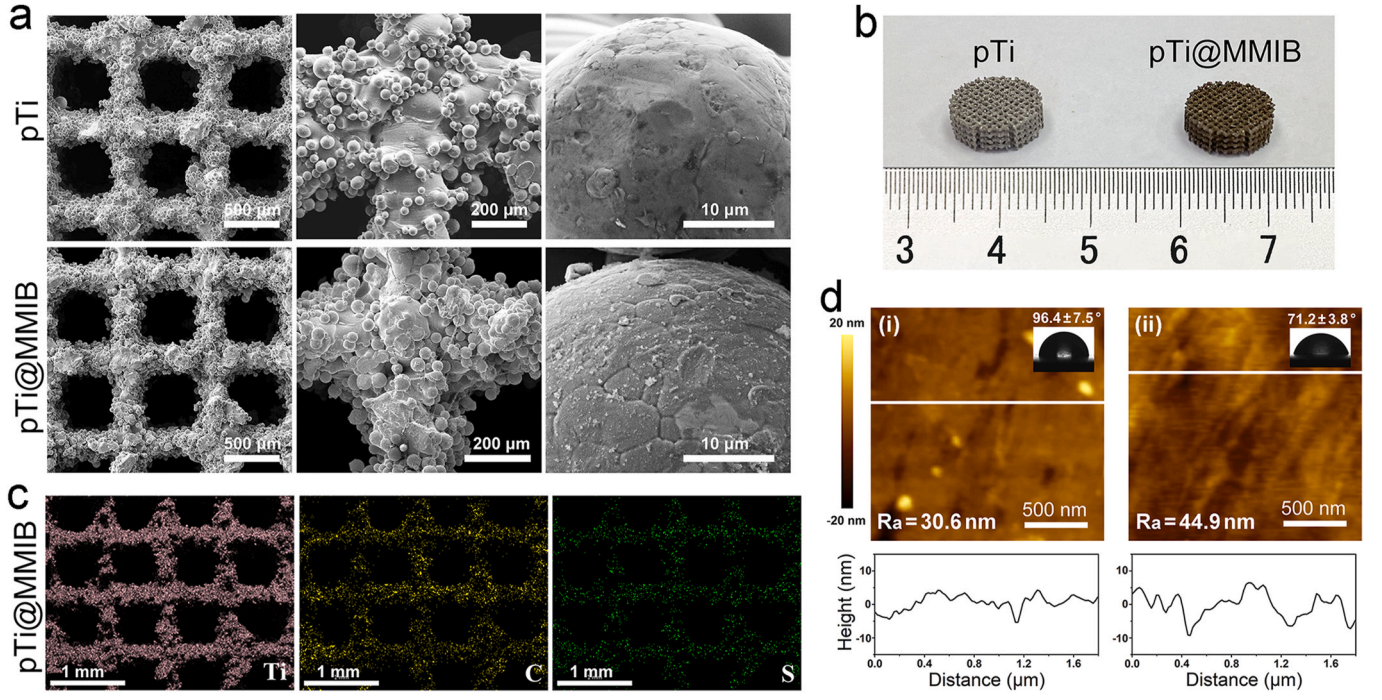

Fig. 1. Characterizations of the pTi@MMIB. (a, b) SEM images (a) and digital pictures (b) of the pTi and pTi@MMIB. (c) SEM image and corresponding elemental mapping (Ti, C, N and S) for pTi@MMIB. (d) AFM images and the corresponding height file of the flat Ti6Al4V surfaces before (i) and after (ii) the MMIB coating; the insert shows the water contact angle of the surfaces.

the wettability of the surfaces increased after the coating, as evidenced by the decreased water contact angle from 96.4 ± 7.5° to 71.2 ± 3.8°. These characterizations demonstrated the successful preparation of the pTi@MMIB prostheses.

3.2. *In vitro* photothermal bactericidal activity

Photothermal treatment offers a sustainable and remotely triggered method to eliminate bacteria on demand via physical hyperthermia. Taking advantage of the high tissue penetration and precise spatial and temporal control of near-infrared (NIR) light, NIR photothermal treatment shows a bright future in next-generation prostheses for non-invasive infection control.

As shown in Fig. 2a and **b**, the ionic liquid coating significantly increased the NIR photothermal conversion of the prosthesis, reaching a level that was approximately 150 % higher than that of bare pTi. When subjected to NIR irradiation, the temperature of pTi@MMIB exhibited rapid and substantial increases, ultimately reaching a maximum temperature change (ΔT) of 43.7 °C at equilibrium in an air environment. In comparison, the bare pTi exhibited a lower ΔT of 30.8 °C under the same NIR irradiation conditions. Further investigation into the NIR photothermal conversion of pTi@MMIB revealed its remarkable sustainability, substantiated by the consistent temperature change curves observed during the NIR "on-off" cycle tests (Fig. 2c).

In the photothermal bactericidal experiments, where the prostheses were immersed into bacteria solutions, it was observed that the temperature of the pTi@MMIB prosthesis at equilibrium decreased slightly to 54.3 °C (compared to 72.3 °C in the air environment), due to the continuous heat transfer to the solution. However, the thermal ablation effect was still sufficient to kill bacteria adhered to the prosthesis effectively via local hyperthermia at the interface. As shown in Fig. 2 d–**i**, nearly 100 % of the bacteria adhered to the pTi@MMIB prosthesis were killed after NIR irradiation, achieving a $\log_{10}$ reduction value (LRV) of 6 against both *E. coli* and *S. aureus*. In contrast, the bare pTi exhibited very weak bactericidal activity, LRV<0.3.

Results of the live/dead assay on a flat Ti6Al4V substrate (the same material as the shaped prosthesis) further validated the robust photothermal bactericidal activity of the ionic liquid coating. As shown in Fig. 3, most of the adhered bacteria on the bare substrate were still alive, even under NIR irradiation. However, the MMIB coating endowed the material with intrinsic bactericidal activity to kill the adhered bacteria, and the activity could be largely enhanced upon NIR irradiation.

Additionally, it is noteworthy that the number of bacteria adhered to the pTi@MMIB surface was ~400 % higher than that on the bare pTi

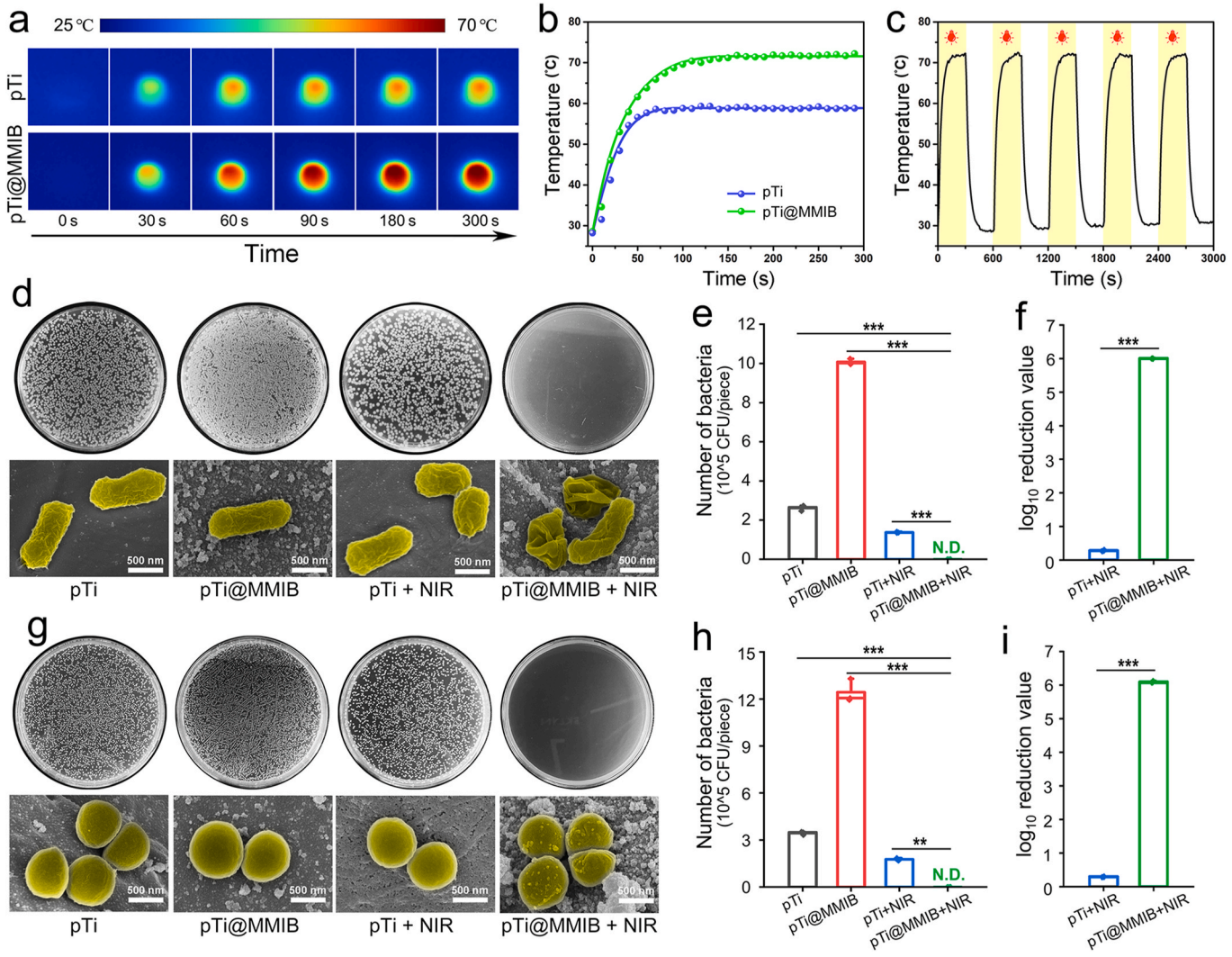

Fig. 2. *In vitro* NIR photothermal bactericidal activity of the pTi@MMIB. (a, b) Infrared thermographic images (a) and temperature change curves (b) of the pTi and pTi@MMIB under NIR irradiation (808 nm, 2 W cm^{-2}). (c) On–off temperature curves for pTi@MMIB under NIR irradiation (808 nm, 2 W cm^{-2}). (d, g) Photographs of the bacterial colonies after the standard plate count assay and SEM images of the adhered bacteria on the prosthesis surfaces. (e, h) Number of adhered bacteria on the prosthesis surfaces. (f, i) NIR photothermal bactericidal activity of pTi and pTi@MMIB. (d–f) for *E. coli*, (g–i) for *S. aureus*. n = 3, **p < 0.01, ***p < 0.001.

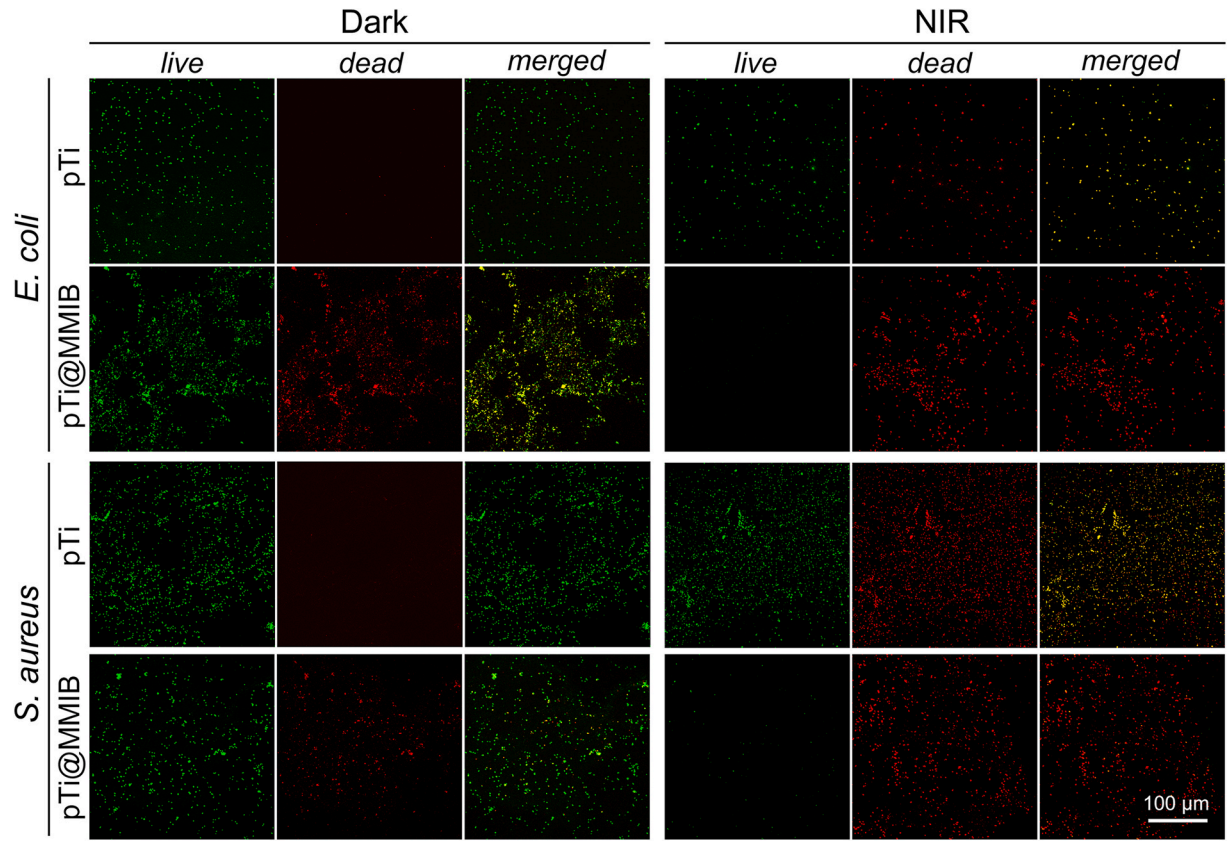

Fig. 3. Fluorescence microscopy images of bacteria adhered on the pTi and pTi@MMIB surfaces, with and without NIR irradiation (808 nm, 2 W cm^{-2}); green and red staining indicate live and dead bacteria, respectively, and bacteria with weak viability appear yellow in the merged images. (For interpretation of the references to color in this figure legend, the reader is referred to the Web version of this article.)

(Figs. 2 and 3), which means the pTi@MMIB could trap planktonic bacteria in the surrounding environment, probably through electrostatic interaction, as the imidazolium ionic liquid coating carried a positive charge while most bacteria are negatively charged. With the synergistic effect of the bacterial recruitment property and photothermal bactericidal activity, our pTi@MMIB prosthesis could trap the surrounding planktonic bacteria and subsequently undergo NIR-triggered photothermal bacteria killing.

Further investigation demonstrated that the bactericidal activity remained consistently effective even after three NIR on/off cycles, confirming the sustainable and durable antibacterial performance of pTi@MMIB. This evidence suggests its potential for long-term infection prevention applications, highlighting its promising role in enhancing prosthetic implant safety and efficacy.

3.3. *In vitro cytocompatibility assessment*

Cytocompatibility of prostheses is a crucial factor to consider in their biomedical applications *in vivo*. Herein, CCK-8 assay and calcein-AM/PI staining were carried out to evaluate the cytotoxicity of both the ionic liquid coating and the NIR irradiation. As shown in Fig. 4a, CCK-8 assay showed that the cell proliferation rate increased gradually with the extension of culture time, and there was no significant difference among the groups. Besides, calcein-AM/PI staining (Fig. 4b) confirmed that the cells in each group were mainly green-stained living cells. Quantitative analysis further supported these findings, revealing that the cell survival rates in the pTi, pTi@MMIB, pTi + NIR, and pTi@MMIB + NIR groups were 92 ± 2 %, 92 ± 2 %, 91 ± 2 %, and 92 ± 2 %, respectively, on the 4th day (Fig. 4c), and 93 ± 1 %, 93 ± 1 %, 92 ± 1 %, and 92 ± 1 %, respectively, on the 7th day (Fig. 4d), with no significant difference among all the groups.

These results dispelled our concerns about the potential cytotoxicity of photothermal treatment. Although NIR irradiation-induced local hyperthermia at the interface may have had some microscopic impact on the adhered cells at the time of treatment, when evaluated over an extended period (days), neither the ionic liquid coating nor NIR irradiation hindered cell viability and proliferation. It might be attributed to the better thermotolerance of mammalian cells than bacteria. They possess a robust system of heat shock proteins and other cellular defenses that can protect them from damage caused by changes in temperature [36–38]. As a result, the cells were able to withstand the photothermal treatment, highlighting the biocompatibility and safety of our pTi@MMIB in bone repair.

3.4. *In vivo antibacterial efficiency assessment*

Many antibacterial surfaces demonstrate promising results *in vitro* but fail to translate into improved outcomes for periprosthetic infections *in vivo* [39–41]. Thus, it is critical to demonstrate the evidence-based performance of our pTi@MMIB in long-term infection prevention. Herein, a bone defect animal model was established by creating a cylindrical defect on the lateral condyle of distal femur using a bone drill. Columnar-shaped prosthesis with precise geometry match with the defect was then implanted. To induce periprosthetic infection, a bacterial suspension containing *S. aureus* and *E. coli* was injected into the medullary cavity through the defects. Infection prevention performance of the prostheses was then evaluated.

As shown in Fig. 5a, the *in vivo* NIR photothermal property of pTi@MMIB remained highly effective after implantation into the distal femur defect. Upon NIR irradiation through the skin and tissues, the temperature of pTi@MMIB increased to 50.8 °C, $\Delta T = 14.9$ °C, which was still much higher than that of bare pTi under the same condition,

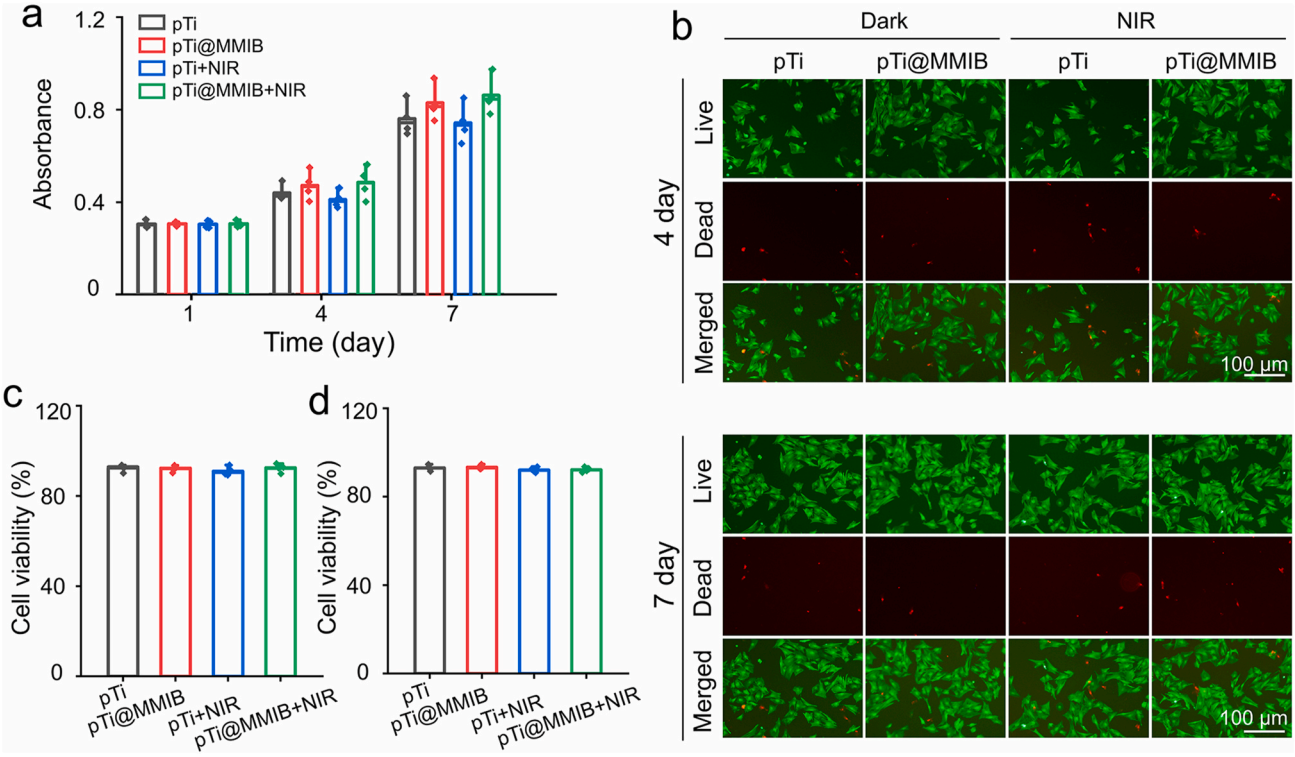

Fig. 4. Cytocompatibility evaluation of the pTi@MMIB and NIR irradiation. (a) CCK-8 proliferation analysis of rBMSCs cultured in the pTi, pTi@MMIB, pTi + NIR, and pTi@MMIB + NIR groups (n = 4). (b) Calcein AM/PI staining of live cells (green) and dead cells (red). (c, d) Quantitative analysis of the cell survival rate on the 4th (c) and 7th (d) day, according to Calcein AM/PI staining (n = 4). (For interpretation of the references to color in this figure legend, the reader is referred to the Web version of this article.)

$\Delta T = 5.8\ ^{\circ}C$. The effective *in-vivo* photothermal performance contributed to the bactericidal activity of the prosthesis to prevent periprosthetic infections. As shown in Fig. 5b, all animals in the pTi@MMIB and pTi@MMIB + NIR groups survived throughout the entire *in-vivo* experiment (12 weeks), whereas 3 in the pTi group and 2 in the pTi + NIR group succumbed to mortality. Blood analysis (Fig. 5 c-**e**) revealed a persistent systemic infection in the pTi and pTi + NIR groups. A significant and continuous increase in the levels of immune cells (white blood cells and neutrophils) and pro-inflammatory cytokine (interleukin 6) was observed throughout the implantation period. In contrast, there was a significant inhibition of such systemic infection in the pTi@MMIB and pTi@MMIB + NIR groups ($p < 0.05$). Especially, the pTi@MMIB + NIR group showed a rapid and efficient anti-infection effect among the groups, and it maintained a continuous control over the systemic infection throughout the experiment. In terms of local periprosthetic infection, which can severely impede osseointegration at the bone–prosthesis interface, Giemsa staining (Fig. 5f) demonstrated a significant presence of bacteria in the pTi and pTi + NIR groups at 12 weeks post-implantation. However, nearly no bacteria were observed in the tissues surrounding the prosthesis interfaces in the pTi@MMIB and pTi@MMIB + NIR groups.

Since the bare pTi prosthesis lacked innate antibacterial properties, an aggravated infection could be observed with increasing time, as indicated by a continuous increase in the WBC count. The pTi + NIR group also showed an incomplete antibacterial effect owing to weak photothermal conversion efficiency. A continuous low-grade infection state was observed in this group, which could impair subsequent bone regeneration. On the other hand, for the pTi@MMIB and pTi@MMIB + NIR groups, the MMIB coating possessed both bacterial recruitment property and intrinsic bactericidal activity, which allowed the prosthesis to capture and confine bacteria around the interface, preventing their spread and exerting continuous bactericidal effects. When combined with NIR irradiation, the pTi@MMIB exhibited a more efficient and rapid sterilization effect. It was observed in Fig. 5f that the pTi@MMIB + NIR group showed a significant reduction in bacterial counts at the 12th week (indicated by the red arrows), promising our antibacterial prosthesis in periprosthetic infection prevention.

3.5. Osseointegration

Bacterial infections on the prosthesis can significantly hinder the process of osseointegration. Thus, herein, the osseointegration performance of the pTi@MMIB prosthesis was evaluated at 12 weeks post-implantation. Benefiting from the perfect geometry and mechanics match achieved through 3D-printing-based precision manufacturing, along with the effective anti-infection performance provided by our ionic liquid coating, the pTi@MMIB + NIR group exhibited outstanding osseointegration performance in the animal experiments.

Macroscopically, the prosthesis interfaces in the pTi@MMIB + NIR group exhibited excellent fixation to the lateral condyle of the distal femur, with a normal and smooth bone surface (Fig. 6a). In contrast, varying degrees of hyperplasia, fibrosis, and necrosis were observed in other groups, indicating the detrimental impact of periprosthetic infection on the local bone structure. To visualize the bone regeneration around the prostheses, micro-CT scanning was performed. The 3D reconstructed images (Fig. 6b) demonstrated that the pTi@MMIB + NIR group showed the highest efficiency in promoting the formation of new bone among all the groups. Compared with other groups, more bone tissue (indicated by the yellow color) was regenerated around the prosthesis interfaces and in the micropores in this group. Quantitative analysis (Fig. 6 c–**f**) revealed that the pTi@MMIB + NIR group exhibited significantly higher values of bone volume/tissue volume ratio (BV/TV), trabecular thickness (Tb. Th), and trabecular number (Tb. N), as well as a lower value of trabecular separation (Tb. Sp), when compared with other groups, indicating the best osseointegration performance for the pTi@MMIB + NIR.

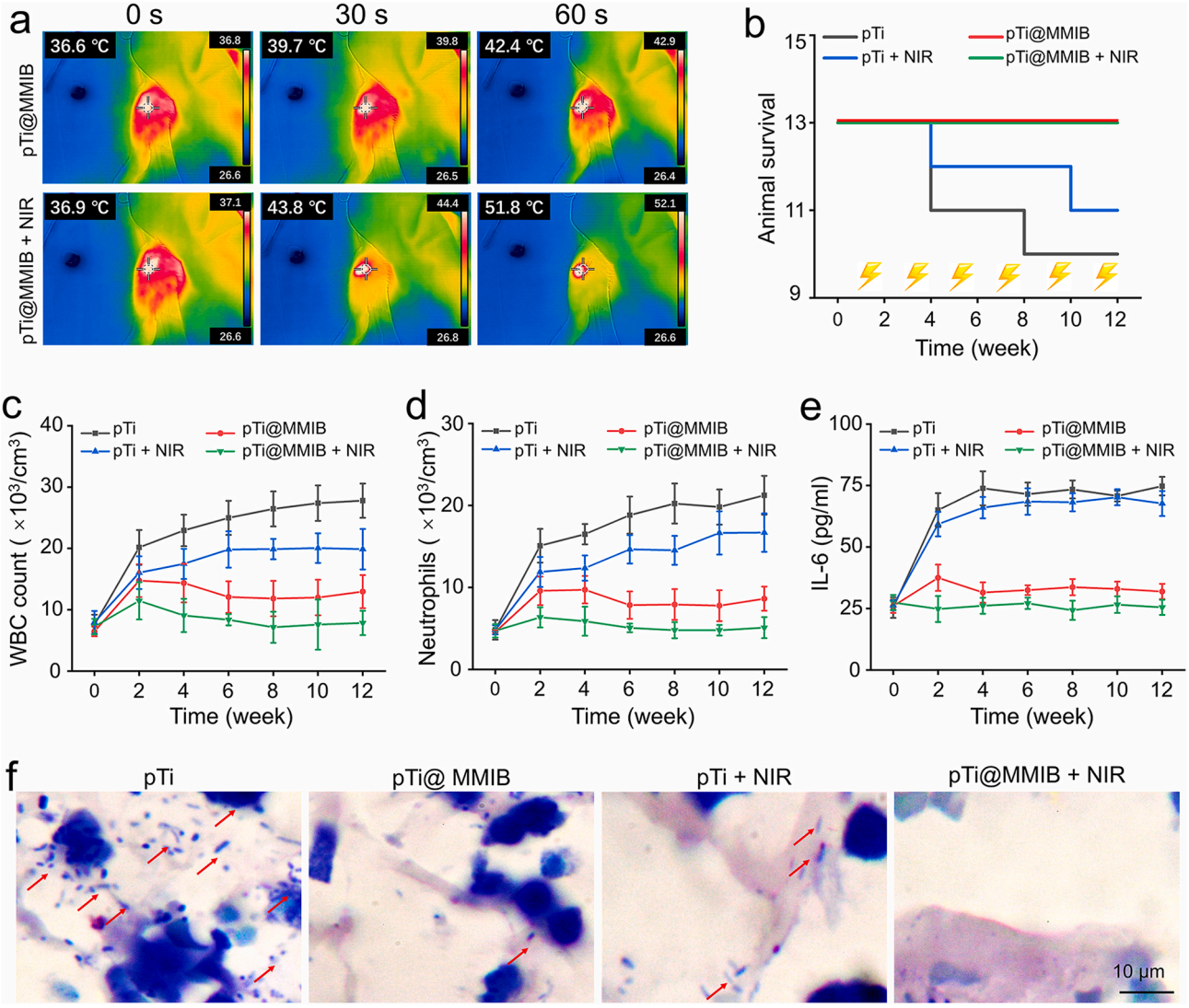

Fig. 5. *In vivo* anti-infection performance of the pTi@MMIB. (a) Temperature change of the implanting pTi and pTi@MMIB under NIR irradiation (808 nm, 2 W cm^{-2}). (b) The survival of the animals during the entire experiment. (c) WBC count in the peripheral blood evaluates the severity of systemic infection (n = 5). (d) Neutrophils count in the peripheral blood after different time of treatment (n = 5). (e) IL-6 content after different time of treatment (n = 5). (f) Giemsa staining shows bacterial contamination in the tissue around the prosthesis interfaces (red arrows indicate bacteria). (For interpretation of the references to color in this figure legend, the reader is referred to the Web version of this article.)

Non-decalcified histology (Fig. 6g) further demonstrated that in the pTi@MMIB + NIR group, regenerated bone tissue almost completely surrounded the prosthesis interface and partially grew into the micropores. In contrast, a large amount of yellow pus was observed in the micropores in the pTi and pTi + NIR groups, and regenerated bone tissue around the prosthesis interfaces was very limited. Biomechanical push-out test demonstrated the highest bonding strength at the prosthesis–bone interface for the pTi@MMIB + NIR group (Fig. 6h). The maximum loading value in this group was measured to be 431 ± 178 N, which was significantly higher than those in other groups. In addition, dynamic histomorphometric analysis indicated the highest mineral apposition rate (MAR) in the pTi@MMIB + NIR group (Fig. 6i and **j**).

These results suggest that the combination of MMIB coating and NIR irradiation endowed the 3D printed pTi prosthesis with the capability to control infections efficiently and sustainably, paving the way for successful osseointegration. Finally, the biological safety of the pTi@MMIB + NIR was evaluated. As shown in Fig. 7, histological analysis revealed that the main organs (heart, liver, spleen, lung, and kidney) of the rabbits exhibited normal characteristics without any signs of toxic reactions, validating the biosafety of our prosthesis with synergistic antibacterial system for *in vivo* applications.

Certainly, when considering a translational solution, it is critical to take into account potential risks of the pTi@MMIB. Although the intrinsic bactericidal activity of the coating could enable pTi@MMIB to kill the adhered bacteria to a certain degree during the early stages after prosthesis implantation, it should be noted that at high bacteria loadings, the bacterial recruitment property of the MMIB coating might lead to higher bacterial adhesion. When NIR irradiation is not applied, the number of survival live bacteria might be increased compared with the bare prosthesis since the intrinsic bactericidal activity may not be sufficient. However, if NIR irradiation is applied blindly, patient compliance will be critical due to the hyperthermia effect. Therefore, it is necessary to combine the pTi@MMIB with clinical diagnosis and advanced detection techniques for periprosthetic infection monitoring, so that the timing of NIR intervention could be directed more precisely. For example, i) Clinical diagnosis is required to direct the timing of NIR irradiation, the wound condition assessing (redness, swelling, heat, pain, etc.) and hematological examination (such as white blood cell count and neutrophils count in peripheral blood) should be carried out to check for signs of periprosthetic infection. ii) Advanced in-situ

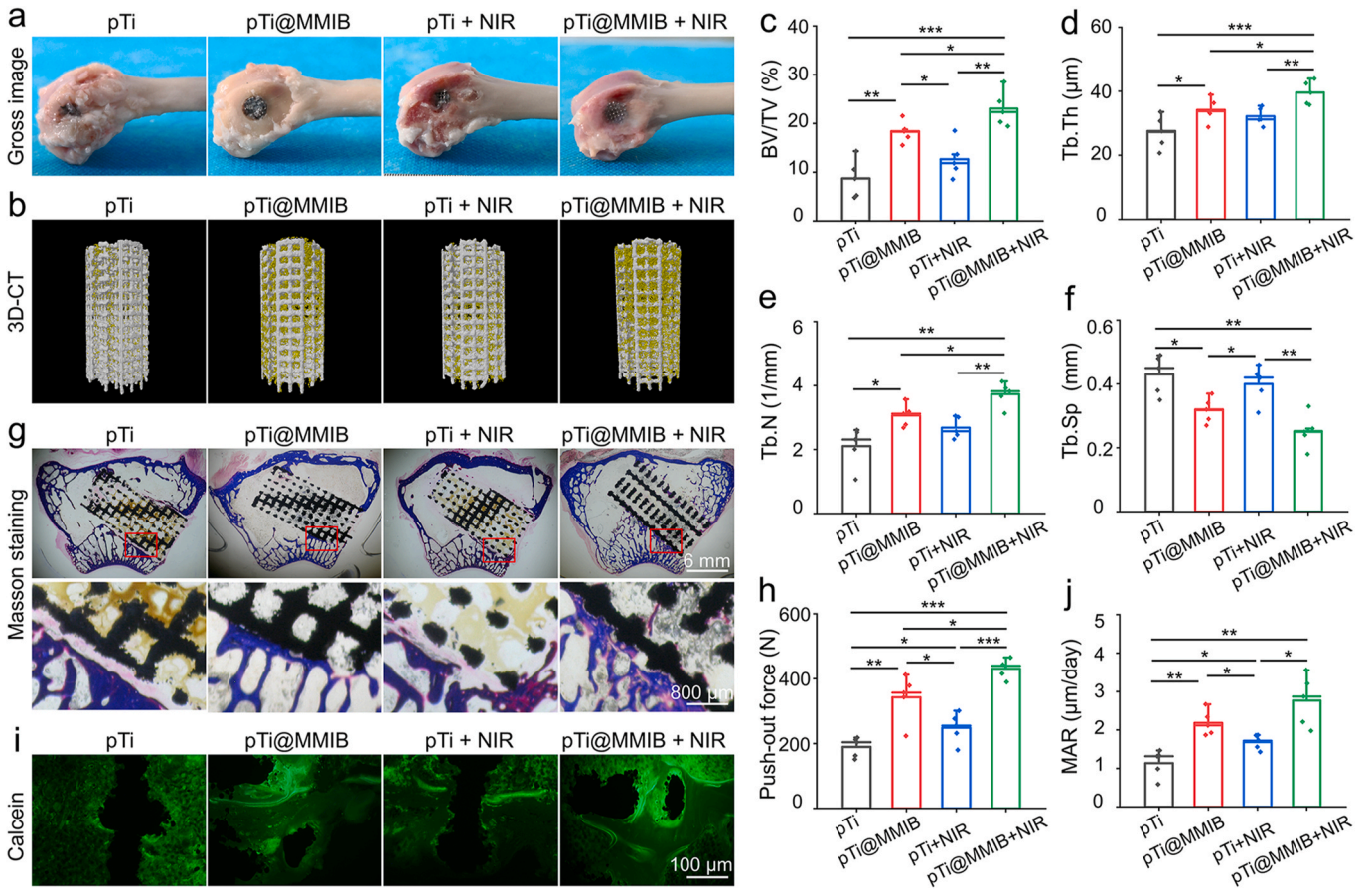

Fig. 6. *In vivo* bone regeneration and osseointegration assessment around the prosthesis interfaces. (a) Gross view of the lateral condyle of distal femurs. (b) 3D reconstruction images of the prosthesis (white) and regenerated bone tissue (yellow). (c–f) Bone morphometric analysis of bone volume/tissue volume (BV/TV) (c), trabecular number (Tb·N) (d), trabecular bone thickness (Tb·Th) (e), trabecular separation (Tb.Sp) (f) according to Micro-CT at 12 weeks post-implantation. (g) Representative histological images of Masson staining (the black areas indicate the pTi prosthesis, the blue areas indicate the bone, and the yellow areas indicate pus). (h) Biomechanical evaluation by pull-out testing to study the osseointegration between the prosthesis interfaces. (i) Representative images of calcein fluorescence double-labelling of bone regeneration around the prosthesis interfaces. (j) Mineral apposition rate (MAR) by calcein fluorescence double labelling (n = 5, *p < 0.05, **p < 0.01, ***p < 0.001). (For interpretation of the references to color in this figure legend, the reader is referred to the Web version of this article.)

detection techniques are highly desired for periprosthetic infection monitoring so that the timing of NIR intervention could be directed in an even more precise way.

4. Conclusion

In summary, the pTi@MMIB prosthesis proposed in this study offers a promising solution for simultaneously preventing periprosthetic infection and promoting osseointegration. 3D-printing-based precision manufacturing enables the creation of personalized pTi prostheses with perfect geometry and mechanics match to each individual patient's anatomy. And our imidazolium ionic liquid coating equips the personalized prostheses with the unique ability to fight against periprosthetic infection on demand using non-invasive NIR irradiation, which is a significant revolution over traditional methods that rely heavily on antibiotic administration or invasive revision surgeries. Overall, the multifunctional prosthesis proposed in this study represents great advancement in the field of orthopedics and has the potential to revolutionize the way to prevent periprosthetic infection. We believe this technology will inspire further innovation and accelerate the development of next-generation prostheses, ultimately benefiting patients around the world.

As we look toward the future, further studies will be necessary to enhance the coating technique in more detail to address engineering issues, such as the coating uniformity and stability, before its practical applications can be realized. Besides, the development of in-situ detection techniques for periprosthetic infection monitoring are highly desired to direct the timing of NIR intervention more precisely. In additional, incorporating microscale heating techniques, such as nanosecond pulsed NIR irradiation, will enable more accurate photothermal control to create highly localized hyperthermia (molecular level) at the prosthesis interface for further enhancing patient compliance. When combined with these advanced technologies, we can further regulate the race between host tissue cells and bacteria on these smart prostheses even more precisely, advancing bone repair into the era of precision medicine.

CRediT authorship contribution statement

Zuhao Li: Writing – review & editing, Writing – original draft, Methodology, Investigation, Formal analysis, Data curation, Conceptualization. **Lunqiang Jin:** Writing – review & editing, Methodology, Investigation, Funding acquisition, Formal analysis, Data curation, Conceptualization. **Xijing Yang:** Methodology, Investigation, Formal analysis, Data curation. **He Liu:** Methodology, Investigation, Data curation. **Shengxu Qian:** Methodology, Investigation. **Zhonghan Wang:** Investigation, Formal analysis, Data curation. **Jiaqi Liu:** Investigation, Formal analysis, Data curation. **Jingxia Wang:** Investigation, Funding acquisition. **Junjun Chen:** Investigation. **Baihai Su:** Supervision, Funding acquisition. **Chaorong Peng:** Supervision, Funding

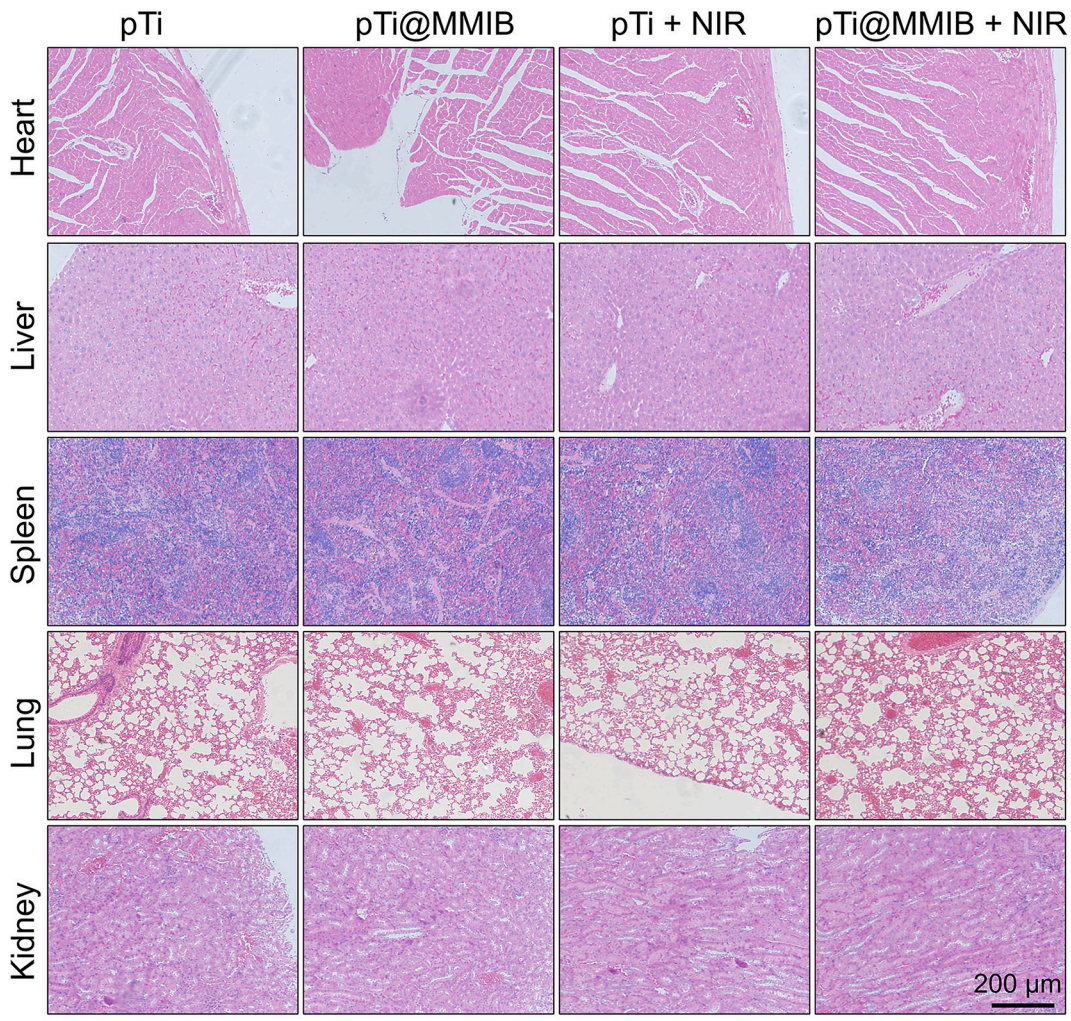

Fig. 7. Representative histological H&E staining images of the main organs taken from the different groups three months after prosthesis implantation.

acquisition. **Jincheng Wang:** Supervision. **Zhenqiang Shi:** Writing – review & editing, Writing – original draft, Supervision, Project administration, Methodology, Investigation, Funding acquisition, Formal analysis, Data curation, Conceptualization.

Declaration of competing interest

The authors declare that they have no known competing financial interests or personal relationships that could have appeared to influence the work reported in this paper.

Data availability

Data will be made available on request.

Acknowledgements

This work was financially sponsored by Sichuan Science and Technology Program (2021YFS0092, 2021JDRC0018, 2022NSFSC1936, 2022YFSY0003, and 2023YFQ0106), Liaoning Province Doctoral Initiation Fund (2022-BS-015), Postgraduate Innovation Research Program of Jilin University (4190214223Q0), the Fellowship China Postdoctoral Science Foundation (2021M692313), Interdisciplinary of Medicine and Engneeering Foundation of Shanghai Jiaotong University (YG2024QNA21) is belongs to the Fundamental Research Funds for the Central Universities, (YG2024QNA21 and DUT24RC(3)013).

Appendix A. Supplementary data

Supplementary data to this article can be found online at https://doi.org/10.1016/j.mtbio.2024.101076.

References

[1] G.L. Koons, M. Diba, A.G. Mikos, Materials design for bone-tissue engineering, Nat. Rev. Mater. 5 (2020) 584–603.
[2] G. Zhang, Y. Yang, J. Shi, X. Yao, W. Chen, X. Wei, X. Zhang, P.K. Chu, Near-infrared light II - assisted rapid biofilm elimination platform for bone implants at mild temperature, Biomaterials 269 (2021) 120634.
[3] M. Caldwell, M. Hughes, F. Wei, C. Ngo, R. Pascua, A.S. Pugazhendhi, M. J. Coathup, Promising applications of D-amino acids in periprosthetic joint infection, Bone Research 11 (1) (2023) 14.
[4] J. Porrino, A. Wang, A. Moats, H. Mulcahy, K. Kani, Prosthetic joint infections: diagnosis, management, and complications of the two-stage replacement arthroplasty, Skeletal Radiol. 49 (6) (2020) 847–859.
[5] R.E. Delanois, J.B. Mistry, C.U. Gwam, N.S. Mohamed, U.S. Choksi, M.A. Mont, Current epidemiology of revision total knee arthroplasty in the United States, J. Arthroplasty 32 (9) (2017) 2663–2668.
[6] Z. Li, Y. Zhao, Z. Wang, M. Ren, X. Wang, H. Liu, Q. Lin, J. Wang, Engineering multifunctional hydrogel-integrated 3D printed bioactive prosthetic interfaces for osteoporotic osseointegration, Adv. Healthcare Mater. 11 (11) (2022) 2102535.
[7] B. Nie, S. Huo, X. Qu, J. Guo, X. Liu, Q. Hong, Y. Wang, J. Yang, B. Yue, Bone infection site targeting nanoparticle-antibiotics delivery vehicle to enhance treatment efficacy of orthopedic implant related infection, Bioact. Mater. 16 (2022) 134–148.
[8] M. Mirkhalaf, Y. Men, R. Wang, Y. No, H. Zreiqat, Personalized 3D printed bone scaffolds: a review, Acta Biomater. 156 (2022) 110–124.

[9] R. Tejero, E. Anitua, G. Orive, Toward the biomimetic implant surface: biopolymers on titanium-based implants for bone regeneration, Prog. Polym. Sci. 39 (7) (2014) 1406–1447.
[10] Z. Wang, L. Han, Y. Zhou, J. Cai, S. Sun, J. Ma, W. Wang, X. Li, L. Ma, The combination of a 3D-Printed porous Ti–6Al–4V alloy scaffold and stem cell sheet technology for the construction of biomimetic engineered bone at an ectopic site, Materials Today Bio 16 (2022) 100433.
[11] X. Pei, L. Wu, C. Zhou, H. Fan, M. Gou, Z. Li, B. Zhang, H. Lei, H. Sun, J. Liang, Q. Jiang, Y. Fan, X. Zhang, 3D printed titanium scaffolds with homogeneous diamond-like structures mimicking that of the osteocyte microenvironment and its bone regeneration study, Biofabrication 13 (1) (2020) 015008.
[12] Y. Zhao, S. Song, D. Wang, H. Liu, J. Zhang, Z. Li, J. Wang, X. Ren, Y. Zhao, Nanozyme-reinforced hydrogel as a H2O2-driven oxygenator for enhancing prosthetic interface osseointegration in rheumatoid arthritis therapy, Nat. Commun. 13 (1) (2022) 6758.
[13] Z. Li, H. Bai, Z. Wang, Y. Liu, M. Ren, X. Wang, W. Gao, Q. Li, M. Wu, H. Liu, J. Wang, Ultrasound-mediated rapamycin delivery for promoting osseointegration of 3D printed prosthetic interfaces via autophagy regulation in osteoporosis, Mater. Des. 216 (2022) 110586.
[14] J. Huang, F. Xie, X. Tan, W. Xing, Y. Zheng, C. Zeng, Treatment of osteosarcoma of the talus with a 3D-printed talar prosthesis, J. Foot Ankle Surg. 60 (1) (2021) 194–198.
[15] G. Beltrami, A.M. Nucci, A. Tamburini, M. Innocenti, Custom-made 3D-printed prosthesis and free vascularised fibula for humeral reconstruction after osteosarcoma resection in a 13-year-old patient, BMJ Case Rep 14 (5) (2021) e240726.
[16] W. Luo, L. Huang, H. Liu, W. Qu, X. Zhao, C. Wang, C. Li, T. Yu, Q. Han, J. Wang, Y. Qin, Customized knee prosthesis in treatment of giant cell tumors of the proximal tibia: application of 3-dimensional printing technology in surgical design, Med. Sci. Mon. Int. Med. J. Exp. Clin. Res. 23 (2017) 1691–1700.
[17] E. Lebaudy, S. Fournel, P. Lavalle, N.E. Vrana, V. Gribova, Recent advances in antiinflammatory material design, Adv. Healthcare Mater. 10 (1) (2021) 2001373.
[18] S. Ghosh, M. Sinha, R. Samanta, S. Sadhasivam, A. Bhattacharyya, A. Nandy, S. Saini, N. Tandon, H. Singh, S. Gupta, A. Chauhan, K.K. Aavula, S.S. Varghese, P. Shi, S. Ghosh, M.K. Garg, T. Saha, A. Padhye, S. Ghosh, H.L. Jang, S. Sengupta, A potent antibiotic-loaded bone-cement implant against staphylococcal bone infections, Nat. Biomed. Eng. 6 (10) (2022) 1180–1195.
[19] G. Pariza, C.I. Mavrodin, I. Antoniac, Dependency between the porosity and polymeric structure of biomaterials used in hernia surgery and chronic mesh - infection, Mater. Plast. 52 (4) (2015) 484–486.
[20] G.L. Koons, M. Diba, A.G. Mikos, Materials design for bone-tissue engineering, Nat. Rev. Mater. 5 (8) (2020) 584–603.
[21] R. Agarwal, A.J. García, Biomaterial strategies for engineering implants for enhanced osseointegration and bone repair, Adv. Drug Deliv. Rev. 94 (2015) 53–62.
[22] Y. Zhao, Z. Li, S. Song, K. Yang, H. Liu, Z. Yang, J. Wang, B. Yang, Q. Lin, Skin-inspired antibacterial conductive hydrogels for epidermal sensors and diabetic foot wound dressings, Adv. Funct. Mater. 29 (31) (2019) 1901474.
[23] Z. Li, C. Wang, C. Li, Z. Wang, F. Yang, H. Liu, Y. Qin, J. Wang, What we have achieved in the design of 3D printed metal implants for application in orthopedics? Personal experience and review, Rapid Prototyp. J. 24 (8) (2018) 1365–1379.
[24] Z.Q. Shi, H.F. Ji, H.C. Yu, X.L. Huang, W.F. Zhao, S.D. Sun, C.S. Zhao, Engineering polyethersulfone hollow fiber membrane with improved blood compatibility and antibacterial property, Colloid Polym. Sci. 294 (2) (2016) 441–453.
[25] Z.Q. Shi, Y.T. Cai, J. Deng, W.F. Zhao, C.S. Zhao, Host–guest self-assembly toward reversible thermoresponsive switching for bacteria killing and detachment, ACS Appl. Mater. Interfaces 8 (36) (2016) 23523–23532.
[26] L. Jin, Z. Shi, X. Zhang, X. Liu, H. Li, J. Wang, F. Liang, W. Zhao, C. Zhao, Intelligent antibacterial surface based on ionic liquid molecular brushes for bacterial killing and release, J. Mater. Chem. B 7 (36) (2019) 5520–5527.
[27] C.N. Kelly, A.T. Miller, S.J. Hollister, R.E. Guldberg, K. Gall, Design and structure–function characterization of 3D printed synthetic porous biomaterials for tissue engineering, Adv. Healthcare Mater. 7 (7) (2018) 1701095.
[28] H. Bai, Y. Cui, C. Wang, Z. Wang, W. Luo, Y. Liu, Y. Leng, J. Wang, Z. Li, H. Liu, 3D printed porous biomimetic composition sustained release zoledronate to promote osseointegration of osteoporotic defects, Mater. Des. 189 (2020) 108513.
[29] H. Bai, Y. Zhao, C. Wang, Z. Wang, J. Wang, H. Liu, Y. Feng, Q. Lin, Z. Li, H. Liu, Enhanced osseointegration of three-dimensional supramolecular bioactive interface through osteoporotic microenvironment regulation, Theranostics 10 (11) (2020) 4779–4794.
[30] Z. Li, C. Liu, B. Wang, C. Wang, Z. Wang, F. Yang, C. Gao, H. Liu, Y. Qin, J. Wang, Heat treatment effect on the mechanical properties, roughness and bone ingrowth capacity of 3D printing porous titanium alloy, RSC Adv. 8 (22) (2018) 12471–12483.
[31] Z. Li, C. Wang, C. Li, Z. Wang, F. Yang, H. Liu, Y. Qin, J. Wang, What we have achieved in the design of 3D printed metal implants for application in orthopedics? Personal experience and review, Rapid Prototyp. J. 24 (8) (2018) 1365–1379.
[32] Z. Chen, X. Yan, S. Yin, L. Liu, X. Liu, G. Zhao, W. Ma, W. Qi, Z. Ren, H. Liao, M. Liu, D. Cai, H. Fang, Influence of the pore size and porosity of selective laser melted Ti6Al4V ELI porous scaffold on cell proliferation, osteogenesis and bone ingrowth, Mater. Sci. Eng., C 106 (2020), 110289-110289.
[33] S. Pan, J. Yin, L. Yu, C. Zhang, Y. Zhu, Y. Gao, Y. Chen, 2D MXene-integrated 3D-printing scaffolds for augmented osteosarcoma phototherapy and accelerated tissue reconstruction, Adv. Sci. 7 (2) (2020) 1901511.
[34] Y. Feng, D. Wu, J. Knaus, S. Keßler, B. Ni, Z. Chen, J. Avaro, R. Xiong, H. Cölfen, Z. Wang, A bioinspired gelatin–amorphous calcium phosphate coating on titanium implant for bone regeneration, Adv. Healthcare Mater. 12 (20) (2023) 220341.
[35] Z. Shi, L. Jin, C. He, Y. Li, C. Jiang, H. Wang, J. Zhang, J. Wang, W. Zhao, C. Zhao, Hemocompatible magnetic particles with broad-spectrum bacteria capture capability for blood purification, J. Colloid Interface Sci. 576 (2020) 1–9.
[36] F. Wang, Y. Shi, P Ho, E.G. Zhao, C. Kam, Q. Zhang, X. Zhao, Y. Pan, S. Chen, An AIE-active bacterial inhibitor and photosensitizer for selective imaging, killing, and photodynamic inactivation of bacteria over mammalian cells, Bioengineering & Translational Medicine 8 (6) (2023) e10539.
[37] M. Liu, B. Chu, R. Sun, J. Ding, H. Ye, Y. Yang, Y. Wu, H. Shi, B. Song, Y. He, H. Wang, J. Hong, Antisense oligonucleotides selectively enter human-derived antibiotic-resistant bacteria through bacterial-specific ATP-binding cassette sugar transporter, Adv. Mater. 35 (28) (2023) 2300477.
[38] L. Zheng, Y. Zhu, Y. Sun, S. Xia, S. Duan, B. Yu, J. Li, F.J. Xu, Flexible modulation of cellular activities with cationic photosensitizers: insights of alkyl chain length on reactive oxygen species antimicrobial mechanisms, Adv. Mater. 35 (35) (2023) 2302943.
[39] X. Liu, C. Bao, H.H.K. Xu, J. Pan, J. Hu, P. Wang, E. Luo, Osteoprotegerin gene-modified BMSCs with hydroxyapatite scaffold for treating critical-sized mandibular defects in ovariectomized osteoporotic rats, Acta Biomater. 42 (2016) 378–388.
[40] C.L. Romanò, G. Manzi, N. Logoluso, D. Romanò, Value of debridement and irrigation for the treatment of peri-prosthetic infections. A systematic review, Hip international : the journal of clinical and experimental research on hip pathology and therapy 22 (Suppl 8) (2012) S19–S24.
[41] Q.Q. Yao, J. Zhou, C.Z. Jiang, J.S. Sui, J.Y. Li, Y. Xu, X.L. Wu, N.Q. Liu, Z. Buser, L. M. Wang, Mechanical and in vitro antibacterial properties of a porous Ti-6Al-4V scaffold combined with vancomycin-loaded polymethyl methacrylate by three-dimensional printing, Journal of Biomaterials and Tissue Engineering 8 (5) (2018) 740–749.